Technical Memo

ECMWF
European Centre for Medium-Range Weather Forecasts

867

Assimilating high resolution remotely sensed soil moisture into a distributed hydrologic model to improve runoff prediction

David Mason[1], Javier Garcia-Pintado[2], Hannah Cloke[1,3], Sarah Dance[1], Joaquin Muñoz-Sabater[4].

[1] University of Reading, UK, [2] University of Bremen, Germany, [3] Uppsala University, Sweden, [4] ECMWF, Reading, UK

June 2020

Series: ECMWF Technical Memoranda

A full list of ECMWF Publications can be found on our website under:
http://www.ecmwf.int/en/publications

Contact: library@ecmwf.int

Abstract

The susceptibility of a catchment to flooding during an extreme rainfall event is affected by its soil moisture condition prior to the event. A study to improve the state vector of a distributed hydrologic model by assimilating high resolution remotely sensed soil moisture is described. The launch of Sentinel-1 has stimulated interest in measuring soil moisture at high resolution suitable for hydrological studies using Synthetic Aperture Radars (SARs). The advantages of using SAR soil moisture in conjunction with land cover data are considered. These include the ability to reduce contamination of the surface soil signal due to vegetation, radar artefacts, mixed pixels and land cover classes not providing meaningful soil moistures. Results for 2008 using ASAR data showed that the assimilation of ASAR soil moisture values improved the predicted flows for all images. The improvement was less marked for 2007, probably because the antecedent soil moisture conditions were of reduced importance during the extreme flooding that occurred then. Particularly for 2008, the higher resolution of ASAR data improved predicted flows compared to low resolution ASCAT data that were not disaggregated and limited to the temporal frequency of ASAR. The method is likely to give better results with Sentinel-1 rather than ASAR data due to its higher temporal resolution.

1 Introduction

The susceptibility of a river catchment to flooding during an extreme rainfall event is affected by its soil moisture condition prior to the event (Seneviratne et al. 2010). The antecedent soil moisture affects runoff because it controls the partitioning of rainfall between infiltration and runoff across the catchment. The improved representation of antecedent soil moisture in hydrologic models should therefore improve runoff prediction (Massari et al. 2015). This paper describes a study that has attempted to improve the forecast of a distributed hydrologic model for a set of catchments by assimilating remotely sensed soil moisture (SM) in order to keep the model flow rate predictions on track in readiness for an intense rainfall event.

Despite the fact that soil moisture and runoff may be correlated, it is currently an open question how much assimilation of remotely sensed SM into a hydrologic model can aid runoff prediction in a catchment (Massari et al. 2015; Parajka et al. 2005; Corato et al. 2014; Crow and Ryu 2009). There seem to be a number of reasons for this. Crow and Ryu (2009) point out that, "for very intense rainfall events, antecedent SM conditions may be of minor importance as the infiltration excess overland flow mechanism is dominant and rainfall runs off before it has the opportunity to infiltrate. Also, for catchments lacking rain gauges, the main uncertainty will be due to the error in forecast rainfall rather than that due to soil moisture." As far as the system and experimental design is concerned, performance depends on factors that include the structure of the hydrologic model, the quality of the remotely sensed SM data, and the characteristics of the data assimilation (DA) scheme. For example, "the relationship between antecedent SM and runoff is strongly non-linear and may be unsuited to the application of DA techniques designed for linear models (e.g. Kalman-derived filters and variational techniques)" (Plaza et al. 2012). Massari et al. (2015) have investigated in detail how methodological and morphoclimatic factors such as catchment area, soil type, climatology, rescaling technique, and observation and model error selection may affect the results of the assimilation and may be the cause of the apparent discrepancies seen in the literature.

As discussed in Mason et al. (2016), the particular reason investigated in this study is "the low spatial resolution of the microwave SM data (e.g. from ASCAT (Advanced Scatterometer), AMSR-E (Advanced Microwave Scanning Radiometer) or SMOS (Soil Moisture and Ocean Salinity satellite))

used in many previous studies (Parrens et al. 2012; Brocca et al. 2012a; Brocca et al. 2012b; Lacava et al. 2012) compared to the 1km resolution of a typical hydrologic model. While a SMOS pixel (40x40km) is a lot larger than a typical un-gauged small catchment (say 10x10km), a 1km resolution would allow SM variations within a small catchment to be detected, and would take into account the spatial heterogeneity of hydrological processes. For example, SM contribution to runoff usually depends on distance to channel and local slope, as well as other factors including soil hydraulic conductivity and land cover. While previous studies have downscaled low resolution data, there should be advantages in using a high resolution product.

Vinnikov et al. (1996) investigated the spatial and temporal length scales of SM variability in deeper layers. The authors separated the variability of the SM field into small- and large-scale components. The small-scale component is due to varying topography, soil type and land cover at the local scale. The large-scale component is due to wide-area atmospheric forcing. In the spatial domain, for the 0-10cm soil layer, they found that 30-35% of the total variance was due to small-scale land surface-related variability, and that this had a length scale of tens of meters. On the other hand, the atmospheric-related component had a length scale of 400-800 km. This means that low resolution microwave sensors measure only the large-scale atmospheric-related component of SM variations because they average out the small-scale topographic variations. Wagner et al. (1999) showed that the low correlations found between area-extensive ERS (European Remote Sensing satellite) scatterometer measurements and point field SM measurements must be caused by the small-scale variability of the SM field. High resolution remotely sensed SM measurement should be capable of going at least part of the way towards observing this local variability."

Soil moisture can be measured at higher resolution using active SARs rather than passive sensors and scatterometers. Recently there has been increasing interest in estimating SM at local scales using these sensors (Barrett et al. 2009; Gruber et al. 2013). This interest has been stimulated by the successful launch of the Sentinel-1 constellation. Sentinel-1 is C-band, which penetrates 1 - 2 cm into the soil, and has significantly improved radiometric accuracy compared to existing instruments (Torres et al. 2012). The first satellite of the pair was launched in 2014 and the second in 2016, and the constellation now gives a revisit interval of 6 days at the equator and about 2 days over Europe. Recently Bauer-Marschallinger et al. (2019) have developed a near real-time system for measuring surface SM at 1km resolution on a global basis using the Interferometric Wide Swath mode of Sentinel-1. This system should provide data at high enough resolution for catchment-scale hydrology studies.

The Sentinel-1 launch has been relatively recent, and it has yet to build up a substantive sequence of flood event data that could be used in an analysis. As a result, as discussed in Mason et al. (2016), "ASAR data have been used for this study. ASAR is also C-band, and ASAR Wide Swath (WS) data were acquired from 2003 – 2011, giving a reasonably long data record. ASAR WS has a spatial resolution of approximately 150m (75m pixel size) and a 400km swath width. VV polarisation images were chosen because of their higher capability of vegetation penetration (and hence SM measurement) compared to HH polarisation (Kong and Dorling, 2008). A difficulty with ASAR WS is that the time interval between successive scene acquisitions can be irregular in many areas. For example, in the data set used in this study, there were on average two scenes per month, but in several months there were no useable scenes at all." Even so, the temporally-sparse data from ASAR WS can be used as a surrogate for the more frequently-acquired data that can now be obtained from Sentinel-1 interferometric wide swath mode.

The use of SAR data for rainfall-runoff estimation was first proposed by Jackson et al. (1981). There appears to be only limited literature relating to the use of high resolution SAR SM measurement to improve discharge estimation. Francois et al. (2003) assimilated ERS SAR SM data into a lumped land-surface/hydrologic model using an extended Kalman Filter, and demonstrated that the assimilation of SAR SM improved flood forecasting. Corato et al. (2014) assimilated ASAR WS data into a distributed hydrological model using a particle filter, and found increases in Nash-Sutcliffe efficiency (Nash and Sutcliffe (1970) for SM measurements assimilated between May and September. Cenci et al. (2016a), using a distributed model and a nudging assimilation scheme, showed that assimilation of disaggregated ASCAT SM with simple preprocessing and assimilation techniques can enhance discharge predictions, especially at high flows. Cenci et al. (2016b) extended this system using Sentinel-1A and ASCAT data, and found that Sentinel-1A SM only marginally improved discharge simulations, though results were better at high flows. Bauer-Marschallinger et al (2018) fused two data streams of satellite soil moisture retrieved separately from Sentinel-1 and ASCAT observations, to produce a product (SCATSAR-*SWI*) with temporal and spatial sampling of 1 day and 1km suitable for small scale flood forecasting applications. Azimi et al. (2020) assimilated the SCATSAR-*SWI* product into the SWAT hydrological model and found an improvement in discharge simulation, albeit small compared to simply using ASCAT. Most previous SM studies using high resolution SAR have been aimed at estimating surface soil moisture content (SSMC). Considering ASAR WS data, Gruber et al. (2013) showed that SSMC measurements from ASAR WS match ground measurements better than those from ASCAT. Loew et al. (2006) derived SM from the ASAR WS backscattering cross-section for various agricultural land covers (including grassland), and concluded that SM can be measured to 5.7 vol% over a range 15 – 40 vol%. Mason et al. (2016) provided evidence of a topographic signal in ASAR WS data by comparing SSMC values from low slopes near rivers to those on higher slopes. As noted in Mason et al. (2016), Kong and Dorling (2008) "used a principal component analysis to show that surface roughness, vegetation and topographic effects could be partially separated (see also Verhoest et al. 1998). ASAR WS data have also been used to study SM variations at high resolution in an alpine valley (Greifeneder et al. 2014); to validate SM measurements from passive microwave sensors at a number of Irish sites (Pratola et al. 2014); and to map surface SM over parts of Tunisia (Zribi et al. 2014). Other high resolution SARs have also been applied to SM measurement, for example multi-polarised RADARSAT-2 over wheat-growing areas (Yang et al. 2013), and TerraSAR-X for bare soils moisture over agricultural areas (Aubert et al. 2013). Pauwels et al. (2009) used airborne ESAR L-band SM data to demonstrate that soil hydraulic parameters could be measured using remote sensing. More recently, Bauer-Marschallinger et al. (2019) developed a method using Sentinel-1 data to build a globally deployable soil moisture observation data set with 1 km resolution. At somewhat lower resolution, ASAR global mode data have been used to estimate SM at regional/continental scales in several studies (Pathe et al. 2009; Dostalova et al. 2014)".

A serious difficulty in investigating the advantages of high resolution SM measurements arises from the enormous amounts of data that would have to be processed, which would constitute a formidable computational challenge. As a result, in this study a more limited objective has been set, which can be regarded as a step along the path towards full investigation. This is to determine whether the assimilation of high resolution remotely sensed SM data into a fully distributed hydrologic model is able to improve runoff prediction, in the case where the SM data are used in conjunction with a land cover map. If SM values can be obtained over land cover pixels of low vegetation (e.g. grassland), this may reduce the component of the backscattered signal due to vegetation, which for dense vegetation types may be a significant proportion of the whole. In addition, signals obtained over such land cover are unlikely to be contaminated by radar artefacts such as multiple reflections, shadow and layover. Measurements may

also be eliminated over land cover classes that do not provide meaningful surface SM, including urban, forest, water, desert and snow/ice (Hornacek et al. 2012). Additionally, backscatter contamination problems caused by mixed pixels containing unknown amounts of more than one land cover type within their coverage can be avoided, which would not be the case for low resolution microwave sensors (Loew et al. 2006). In investigating this objective, note that the high resolution of the ASAR data is primarily being exploited to select SM values over low vegetation in conjunction with the land cover map, rather than to perform dense assimilation at high resolution. Due to computing constraints, the density of SM values assimilated is still on the scale of the large- rather than small-scale component of SM variability.

2 Materials and methods

2.1 River catchment information

As described in Mason et al. (2016), "the study area considered covered the catchments of the Severn and Avon rivers in the South West United Kingdom (fig. 1). This included the three main catchments of the Severn, Avon and Teme, and four other sub-catchments. The bounding rectangle of the area is 191 km x 124 km. The southern boundary lies just below the town of Tewkesbury, which lies at the confluence of the Severn, flowing in from the north-west, and the Avon, flowing in from the north-east. The elevation range of the area is 10 – 300m AOD (Above Ordnance Datum), with most of the higher land in the west of the region. The domain includes a number of small catchments less than 100 km^2 in area. The mean slope is 7%, with a slope standard deviation of 8%. In the upland regions, the geology is mainly Ordovician and Silurian shales, while downstream it becomes more varied, with river gravels, marls and sandstones. The surface soil layer is mainly fine textured clay. The predominant land cover types are improved grassland and arable." Each of the differently colored catchments shown in fig. 1 has a gauge at its outflow because the area floods on a reasonably frequent basis.

Figure 1. Severn/Avon catchments and sub-catchments (color table identifies main catchments only).

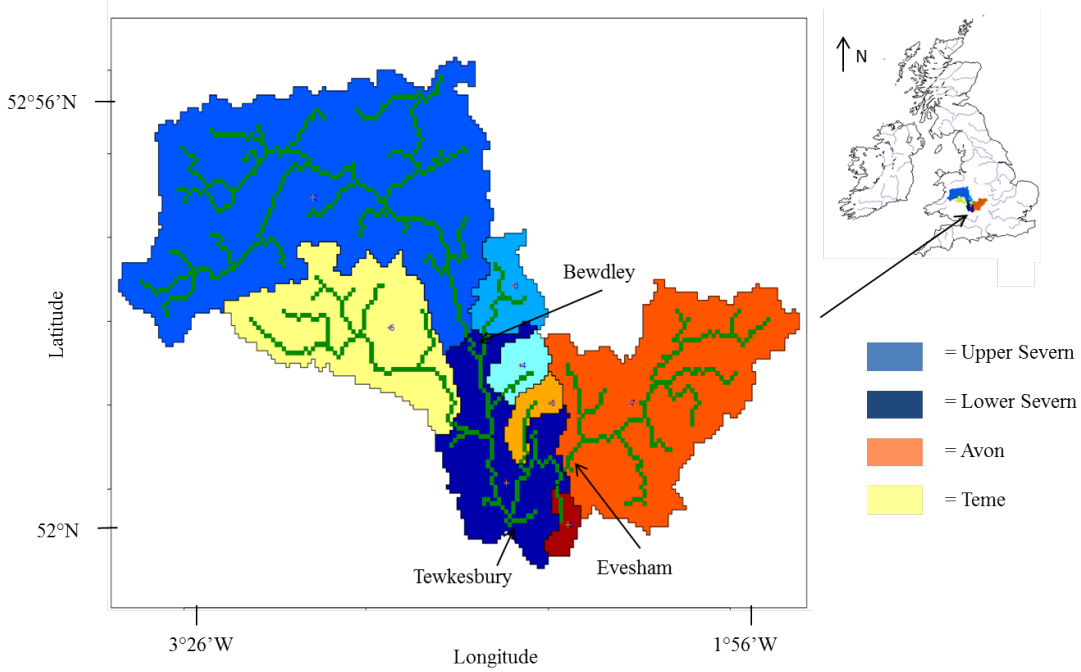

2.2 Methods

2.2.1 Hydrological modelling

2.2.1.1 Distributed hydrological model

We used a hydrologic model based on the rainfall-runoff module for pervious land (PWATER) of the Hydrological Simulation Program FORTRAN (HSPF) (Donigian et al. 1995; Bicknell et al. 1997). HSPF is a lumped model which contains a number of modules for simulating hydrology and associated water quality processes in rural (pervious) and urban (impervious) land surfaces and in streams and well-mixed impoundments.

For this study, a spatially distributed version of the PWATER module, so-called topHSPF, was constructed, in which all model variables are evaluated on a 1 km x 1 km grid and overland flow takes a gridded topography explicitly into account via a cell-to-cell kinematic wave routing for overland flow. For channelized routing, the kinematic wave includes a sub-grid approach similar to that of Neal et al. (2012), assuming rectangular channel cross-sections. In topHSPF, the constitutive functions to simulate evapotranspiration, interception, and infiltration and water distribution in the soil column from the root zone up to groundwater are identical to those in HSPF. Section 4.2(1).3 and Figure 4.2(1).3.2 of Bicknell et al. (1997) describe in detail the constitutive functions and show a flow diagram of the model water movement and storage, respectively. However, in topHSPF all variables are evaluated in a distributed way, allowing for a horizontal and vertical spatial variability in water storage. Accordingly, the model is able to ingest spatiotemporally distributed meteorological forcing, and is suitable for the assimilation of high resolution satellite surface SM information. In the model, precipitation (model variable *supy*) feeds the interception storage (*ceps*), from which there is evaporation (*cepe*) and one outflow (*cepo*) into the surface detention storage (*surs*), or overland storage. Then, the output of the overland storage, *surs*, is divided into four components: surface outflow (*suro*) routed out of the catchment, interflow input (*ifwi*), upper zone inflow (*uzi*), and infiltration (*infil*), which is later available for deeper infiltration. The only difference in the flow diagram of topHSPF with respect the original PWATER, is that the coupling between the cell-to-cell kinematic routing module is via the surface store variable, *surs*, which is explicitly routed so that the overland flow out of each catchment is obtained at the cell corresponding to the catchment outlet. Water balance for overland flow is evaluated for each cell, so that *suro* can be negative. Algorithms in topHSPF are identical to those in the standard HSPF except for the overland flow routing, but they are evaluated on a per-cell basis. There are two other flows out of each catchment, coming from the interflow storage and the active groundwater storage. These two storages consider the balance in the water column at each model cell. There is no explicit lateral routing of the interflow or groundwater (as opposed to the overland flow). Groundwater exfiltration is considered at the catchment scale as the sum of groundwater outflows for all grid cells in the catchment (*agwo*). Interflow outflow (*ifwo*) is similarly obtained by integrating over all cells within the catchment. The model time-step is 15 minutes.

The hydrologic model was forced by distributed precipitation fields and potential evapotranspiration. Precipitation data were obtained from Environment Agency (EA) tipping bucket rain gauge data, available from 2002 to the present. The point data were first integrated over hourly timesteps, then interpolated by Ordinary Kriging (OK) to obtain gridded rainfall estimates at 1 km spatial resolution. To obtain a precipitation ensemble, an ensemble of errors was added to the OK mean estimates. These errors were multiplicative and generated using a log-normal transform in a standardized space from a stochastic unconstrained Monte Carlo simulation of spatially correlated error with a typical correlation

length for the UK of 10 km, as described in Blenkinsop et al. (2017). Further, the errors were also correlated in time to emulate the time propagation of the error covariance in Numerical Weather Prediction (NWP) models. Temporal decorrelation in NWP errors depends on the specific model error dynamics, including factors such as geographical dependence. Here we chose 1 day as temporal correlation scale as a likely reasonable value. Heteroscedasticity was taken into account by scaling the errors with the OK precipitation estimates, so that grid cells with larger precipitations had larger errors. Potential Evapotranspiration (PEVT) datasets were also extracted for the study domain and period from the UK Met. Office MORECS data set (Hough and Jones 1997). No error was added to the potential evapotranspiration forcing, as modelled discharges were fairly insensitive to its variation.

A validation database of discharge series for seven rivers in the Severn-Avon-Teme catchments and sub-catchments was developed with gauge flow data provided by the EA for 2007-2008, corresponding to the available ASAR scenes. The validation period covered the months of May – October during 2007 and 2008, and included three floods, in June 2007, July 2007 (a major flood) and September 2008.

2.2.1.2 Model calibration

The distributed topHSPF hydrologic model was calibrated using flow data for the whole of year 2009, which included a significant flood event. Precipitation and potential evapotranspiration were used as input data, and gauge flow at the outlet of each of the 7 catchments were available as calibration data. Calibration was performed using a simple Monte Carlo run, sampling from prior uniform distributions with common ranges for the model parameters as indicated in the HSPF model documentation. Behavioral ranges of parameters were evaluated according to the Nash-Sutcliffe model efficiency coefficient (NS). The behavioral ranges had some differences among the 7 catchments, but were reasonably close, mostly in the two biggest catchments; the Severn (outlet gauge at Bewdley) and the Avon (outlet gauge at Evesham). For simplicity we considered it sensible to select the run with the highest NS score at Bewdley as the “calibrated” parameter set for all the 7 catchments.

The variables of topHSPF were divided into two sets, state variables and parameters. Model parameters were estimated by calibration prior to assimilation, and are given in Table 1. The state variables (table 2) were distributed in space and time, and formed the state vector that was updated during the assimilation. A full description of all these variables is given in Bicknell et al. (1997).

Table 1. Calibrated values of the parameters of the hydrologic model.

Parameter	**Description**	**Value**	**Calibrated**
uzsn	Upper zone nominal storage capacity (mm)	6.3	Yes
lzsn	Lower zone nominal storage capacity (mm)	15.9	Yes
infilt	Index to the infiltration capacity of the soil (mm.hour^{-1})	1.5	Yes
kvary	Parameter controlling groundwater recession flow (mm^{-1})	0	No
agwr	Groundwater recession rate if kvary = 0 and no inflow (day^{-1})	0 .9	Yes
infexp	Exponent of the infiltration equation	3.1	Yes
infild	Ratio of the maximum to mean infiltration capacity over the land segment	2.0	No
deepfr	Fraction of groundwater that will enter deep (inactive) groundwater, and be lost to HSPF	0.5	No
basetp	Fraction of remaining potential evapotranspiration (ET) that can be satisfied from baseflow	0.0	No
agwetp	Fraction of remaining potential ET that can be satisfied from active groundwater storage	0.0	No
cepsc	Maximum interception storage capacity (mm)	0.09	Yes
intfw	Interflow inflow parameter	7.8	Yes
irc	Interflow recession parameter (day^{-1})	0.9	Yes
lzetp	Lower zone ET parameter	0.7	Yes

Table 2. topHSPF state variables.

State variable	Description
ceps	Interception storage (mm)
surs	Surface (overland) storage (mm)
ifws	Interflow storage (mm)
uzs	Upper zone storage (mm)
lzs	Lower zone storage (mm)
agws	Active groundwater storage (mm)
gwvs	Index to groundwater slope

Fig. 2 shows selected variables in topHSPF for the Severn at Bewdley for the calibration period of 2009 (NS = 0.68). Of particular interest is the Total Runoff and Components plot (fig. 2c). This shows that the dominant contributors were interflow (*ifwo*), and groundwater (*agwo*), while the contribution from direct overland flow (*suro*) was negligible. This was in partial contrast to the prediction of the normal lumped version of HSPF (not shown), which predicted a groundwater flow higher than the more surficial interflow. This results from the explicitly distributed overland flow in topHSPF, which promotes the downstream water transport closer to the surface, increasing the areas contributing to interflow, as relatively less opportunity is given to percolation towards the aquifer. This gave some confidence that the physical representation of the hydrological processes in the distributed case appeared sounder than in the lumped case.

The model *SWI* value was taken to be *uzrat*, the ratio of the upper zone storage *uzs* to the upper zone nominal storage *uzsn* (i.e. *uzrat* = *uzs/uzsn*) (Bicknell et al. 1997). Note that *uzsn* is the upper zone nominal storage capacity, which is less than the upper zone total storage capacity, so that *uzrat* may be greater than 1.

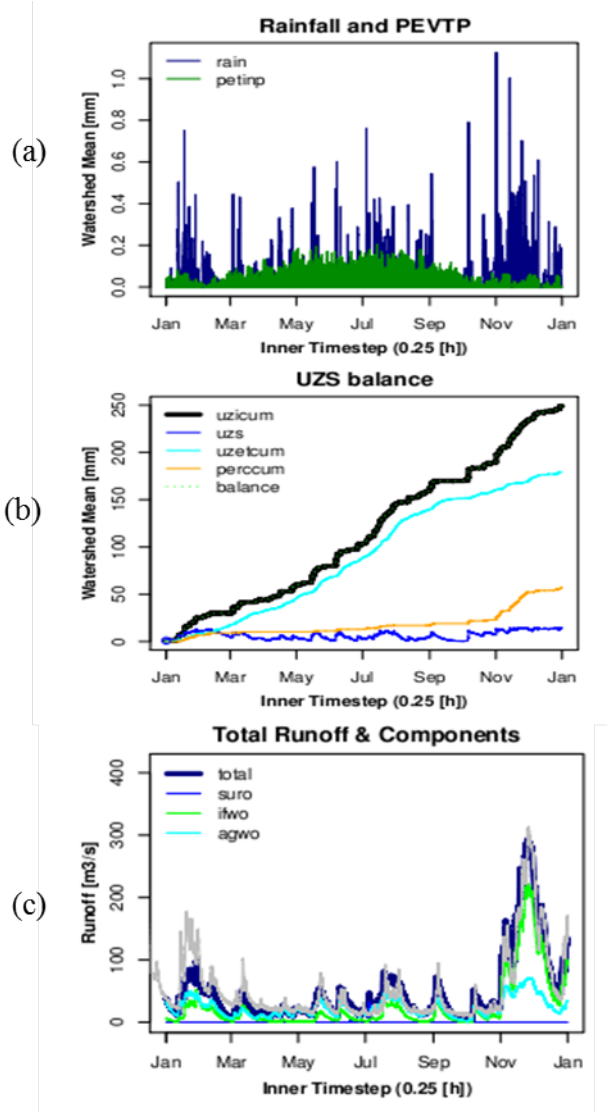

Figure 2. Plots of selected variables in topHSPF for Severn at Bewdley for the calibration period (2009) (a) rainfall and potential evapotranspiration (PEVTP) (petinp = input PEVTP), (b) upper zone storage (uzs) balance (uzicum = cumulative inflow, uzs = upper zone storage, uzetcum = cumulative evapotranspiration, perccum = cumulative percolation - the balance line gives the sum of uzs, uzetcum, and perccum, and matches uzicum as no assimilation is used here), and (c) total predicted runoff and components (suro = surface runoff, ifwo = interflow, agwo = groundwater, grey line = observed gauge flow).

2.2.2 Satellite data processing

2.2.2.1 ASAR

Processing of the ASAR data consisted of a number of steps, further details of which are given in Mason et al. (2016). They included -

- Snow cover masking
- Terrain correction
- Incidence angle normalization
- Calculation of relative surface soil moisture content
- Upscaling to 1km relative surface soil moisture maps
- Profile soil moisture retrieval.

1) *Snow cover masking*. In order to remove the adverse effects of snow cover and frozen soils on surface SM measurement, ASAR WS scenes that were affected were masked out using the L3 8 day MODIS snow product MYD10C2 (Hall et al. 2002).

2) *Terrain correction*. "A Range-Doppler Terrain Correction was applied to the geocoded sub-images of the Severn/Avon domain using the European Space Agency (ESA) NEST (Next ESA SAR toolbox) software and the Shuttle Radar Topography Mission (SRTM) Digital Elevation Model (DEM). Changes in local terrain slopes and aspect with respect to the incident wave will cause significant distortion in the radar backscatter intensities, and Loew et al. (2006) point out that it is mandatory to normalize the image data for terrain-induced backscatter changes"[7].

3) *Incidence angle normalization*. "A local incidence angle normalization was applied for the improved grassland land cover class.

To help cope with the fact that C-band data penetrates only 1-2 cm into the soil, SM was only measured in large homogeneous regions having low local vegetation cover, namely areas of improved grassland. In the subsequent assimilation stage, SM was only assimilated into the hydrologic model in these regions, as it is neither necessary nor typical for a full grid of observations to be present for assimilation to proceed. Pixels of improved grassland in the Severn/Avon region (fig. 3 of Mason et al. 2016) were selected using the CEH Land Cover Map, constructed from high resolution multispectral satellite data (Morton et al. 2011). The original map containing 25m pixels was averaged to produce 75m pixels to correspond to the ASAR WS pixel size. Because the ASAR WS spatial resolution is twice its pixel size, improved grassland pixels were only selected if a central 75m pixel and its border of 25m pixels were all classed as improved grassland. This avoided edge effects and ensured more homogeneous improved grassland pixels, so that problems caused by mixed pixels could be reduced. It also minimized contamination of the radar signal due to multiple reflections, and shadow and layover caused by trees and buildings. Pixels of other land cover types (arable, woodland, urban, water, etc.) were ignored" (Mason et al. 2016). It must be acknowledged that the use of ASAR data only over improved grassland

may limit application of the method over other cover types, and this aspect needs to be investigated further. However, "approximately one-third of the Severn/Avon region is classed as improved grassland, giving a substantial pixel sample size for measurements in this region" (Mason et al. 2016).

"Radar backscatter generally shows a strong dependence on local incidence angle, with backscatter decreasing strongly with increasing incidence angle over sparsely vegetated terrain such as improved grassland (Pathe et al. 2009). Following Loew et al. (2006), a statistical approach was used to normalize the backscattering cross-section to a reference incidence angle of 23°, given an incidence angle range in the ASAR data of 15° - 45°. The SAR image data in homogeneous improved grassland pixels in the Severn/Avon domain were used to derive angular variations of the backscattering cross-section, based on 40 ASAR WS images from 2006-8. In common with other approaches, a simple linear model was fitted to data acquired over this period. The slope β of this was assumed to be constant over time. A value for β of -0.093 ± 0.003 db/degree was found in the regression" (Mason et al. 2016).

4) *Calculation of relative surface soil moisture content (SSMC).* Surficial soil moisture was measured using the change detection technique of Wagner et al. (1999) applied to the ASAR image sequence. "SM measurement using change detection is based on the fact that variations in surface backscatter observed with a short repeat interval should mainly reflect changes in SM, since changes of surface roughness, canopy structure and vegetation biomass will generally occur at longer temporal scales than SM changes. The method estimates the degree of surface water soil saturation, from which the volume of water present in the soil relative to the volume of the soil's pores can be deduced (Hornacek et al. 2012). The change detection method has been shown to perform as well as a number of other methods for detecting SSMC (Gruber et al. 2014)" (Mason et al. 2016). "The relative SSMC m_s is calculated using (Wagner et al. 1999) –

$$m_s = (\sigma^0 - \sigma^0_{dry}) / (\sigma^0_{wet} - \sigma^0_{dry}) \qquad (1)$$

σ^0_{dry} and σ^0_{wet} are assumed to represent dry and wet soil conditions at a pixel respectively" (Mason et al. 2016). The method that was used to calculate σ^0_{dry} and σ^0_{wet} is described in Mason et al. (2016). This involves calculating σ^0_{dry} at a pixel by taking the average of the three lowest values at the pixel from a set of dry images. Similarly, σ^0_{wet} is calculated by taking the average of the three highest values at the pixel from a set of wet images.

5) *Upscaling to 1km relative surface soil moisture maps.* The full resolution relative surface SM images were upscaled to 1 km resolution to match the grid size of the hydrologic model. In this upscaling, the output value at each 1 km pixel was the average of all the 75 m pixel values coinciding with grassland in the 1 km pixel. If the proportion of these 75 m pixels was less than a user-specified fraction, the output value at the 1 km pixel was set to zero.

6) *Profile soil moisture retrieval*. "The relative SSMC m_s is a measure of SM only in the thin surface layer, whereas it is knowledge of the deeper root zone SM that allows the assimilation to update the model SM states at deeper layers. The approach taken here was to derive a soil water index *SWI(t)* from m_s through the application of the exponential filter due to Wagner et al. (1999), so that *SWI* rather than m_s may be assimilated (Brocca et al. 2012a; Brocca et al. 2012b; Lacava et al. 2012). *SWI(t)* ($0 \leq SWI \leq 1$) is calculated for the profile at time t by forming a weighted average of the $m_s(t_i)$ values from the previous i ASAR measurements at time t_i ($t_i \leq t$). Each $m_s(t_i)$ value is weighted by the negative exponential $exp(-(t-t_i)/T)$ (see equation [6] of Wagner et al. 1999). *SWI(t)* is calculated if there is at least one ASAR measurement in the time interval [t-T, t] and at least three measurements in the interval [t-

5T, t]" (Mason et al. 2016). The parameter *T* was estimated to be 11 days by calculating the correlation between the ASAR and model *SWI* values, and selecting the *T* value giving the highest correlation subject to the condition that the potential ASAR *SWI* image set was not overly thinned. Even though the ASAR *SWI i*mages were sparse, they were sufficiently frequent to satisfy the requirements of the filter.

Table 3 shows the days on which ASAR *SWI* measurements were available during the period January 2007 – December 2008. These were mainly in the summer months as snow-affected scenes were removed from the sample. In order to maximize the number of measurements, both descending and ascending ASAR WS scenes were used to calculate *SWI*. Table 3 shows that there were only 20 days on which ASAR *SWI* could be assimilated. Longer runs could have been obtained using the recursive formulation of the exponential filter given in Albergel et al. (2008). But, in the presence of extensive data gaps, it is questionable whether the *SWI* observations generated would have been reliable and worth assimilating. Indeed, it did not seem sensible to predict *SWI* forward in time from the latest ASAR overpass used in the filter, because e.g. if it rained in the T days after this overpass, the hydrologic model solution would take the rainfall into account, but the exponential filter would not. It was decided to apply the filter only at overpass times, and assimilate the *SWI* values at these times.

Table 3. Days with ASAR *SWI* measurements available for 2007-2008.

Date range	Number of days	Days with *SWI* measurements available (dd/mmm/yyyy)			
2007	11	07/Jan/2007, 02/June/2007, 01/Oct/2007,	26/Jan/2007, 15/Jun/2007, 04/Oct/2007,	25/Apr/2007, 21/Jun/2007, 21/Nov/2007	30/May/2007, 23/Jul/2007,
2008	9	30/May/2008, 09/Sep/2008, 04/Oct/2008	13/Jul/2008, 12/Sep/2008,	23/Jul/2008, 15/Sep/2008,	02/Sep/2008, 28/Sep/2008,

7) Data reduction.

Approximately 65% of the 1 km pixels in each ASAR *SWI* image to be assimilated contained at least one ASAR 75m pixel covering grassland. This should provide sufficient resolution to allow SM variations due to local topography to be detected, which may help to take into account the spatial heterogeneity of hydrological processes. As expected, because the hydrologic model is distributed, this large data set resulted in unacceptably long assimilation times to update all variables described in Table 2 (which formed a state vector of order 10^5 long for the given domain) for all ensemble members, using

a 15-processor workstation, which can be considered standard computational resources in regional flood forecast centers at this time.

Nevertheless, the objective of this paper can be studied adequately using a subset of these data. To recap, this objective considers whether there is advantage in measuring high resolution SM combined with a land cover map over single pixels of homogeneous low vegetation cover. This would not be possible for low resolution microwave sensors, and differs from the method used to produce the 1 km-resolution SM product from Sentinel-1 (Bauer-Marschallinger et al. 2019; Hornacek et al. 2012) (see Section 4).

To this end, the data were reduced spatially to a level giving acceptable assimilation times for an image. Two methods of data reduction were used. The first was simply to increase the user-specified proportion of 75 m ASAR pixels covering grassland to 50% in the upscaling of the 75 m ASAR relative SM image to the 1 km SM map. Secondly, an adaptive thinning algorithm due to Ochotta et al. (2005) was applied to the candidate 1 km pixels to reduce their number while retaining their essential information content. The method adopts a top-down clustering approach using a distance metric that combines spatial distance between observations with difference in observation values. Observations with similar spatial positions and relative SM values are grouped into clusters which are approximated by one representative measure (i.e. the mean of the cluster). The thinning ensures that the errors of spatially-contiguous cluster mean *SWI* values are spatially uncorrelated. After the data reduction, typically a few tens of 1 km *SWI* pixels in each ASAR image remained for assimilation.

2.2.2.2 ASAR

Low resolution data from ASCAT were compared to the high resolution data from ASAR in the SM assimilation studies. ASCAT is an active C-band scatterometer on board the EUMETSAT MetOp satellite. MetOp-A ASCAT 25 km resolution surface SM images (H-SAF H25 Metop ASCAT DR2015 SSM time series) of the study domain for 2007-8 (the earliest available) were downloaded from the Technische Universitat Wien Remote Sensing Group site (TU Wien Remote Sensing Group 2016). In the TU-Wien ASCAT processing chain, long-term scatterometer data are used to model the incidence angle dependency of the radar backscattering signal. Knowing the incidence angle dependency, the backscattering coefficients are normalized to a reference incidence angle (Wagner et al. 1999). The relative SM data ranging between 0% and 100% are then derived by scaling the normalized backscattering coefficients between the lowest/highest values corresponding to the driest/wettest soil conditions (Wagner et al. 1999; Naeimi et al. 2009). The ASCAT data have a pixel size of 12.5 km and a mean sampling interval of 1 day.

The ASCAT relative surface SM values were downscaled to1 km pixel size using resampling, to match the resolution of the hydrologic model. It is important to note that these data are unlikely to be as accurate as the ASCAT SM-OBS-2 data used in many other SM studies (e.g. Cenci et al. 2016a). The latter are disaggregated data derived using fine-mesh information from ASAR ScanSAR Global monitoring mode (1 km resolution) (H-SAF 2015). SM-OBS-2 data are available over Europe and other parts of the world, but not over the UK as Global Mode data were never collected there. In addition, these data are only available from 2009.

For ASCAT, the *SWI* values were again estimated from relative surface SM values using the low pass exponential filter. Descending and ascending scenes were treated independently, so that descending ASCAT *SWI* scenes were constructed only from descending ASCAT *SSM* images, and vice versa.

Ideally the ASAR and ASCAT observations should be obtained at the same time of day to avoid differences over to the diurnal cycle (Wagner et al. 1999). The ASCAT descending pass occurs in the morning at a similar time as the ASAR descending pass, while the ASCAT ascending pass is in the evening similar to the ASAR ascending pass. A difficulty was that, because of the limited number of ASAR scenes, both descending and ascending ASAR scenes needed to be used to calculate ASAR *SWI* images. Because the majority of the ASAR scenes were descending, it was decided to use only the descending pass ASCAT *SWI* images in the assimilation. The ASCAT *SWI* images were calculated for the times at which the ASAR *SWI* images had been calculated, so that for each ASAR *SWI* image there was a corresponding ASCAT *SWI* image.

One difference between the ASCAT and ASAR processing was that the ASCAT data did not have the Range-Doppler Terrain correction applied using the SRTM DEM because of the large size of the ASCAT pixels. So ASAR SM values might have more information in them because of this. Another difference was that ASAR data were normalized to an incidence angle of 23°, while ASCAT data were normalized to 40°. However, the regression of backscatter cross-section σ_0 against incidence angle is linear (Pathe et al. 2009) , so while this difference in normalization will affect the ASCAT σ_0 values, it has been assumed that they have all been scaled by the same proportionality constant. This has been taken into account in the rescaling and triple collocation calculations below.

It was also necessary to thin the ASCAT data. This simply involved retaining only those ASCAT 1 km pixels at the same positions as each retained ASAR 1 km pixel, for each *SWI* image. The ASCAT 1 km pixels had already been downscaled from the original 12.5 km pixels, so that it made little sense to apply a more complicated thinning procedure than this to them.

2.2.3 Error estimation

The ASAR and ASCAT *SWI* values, and the model open loop run (i.e. without data assimilation) ensemble mean *SWI* values, all exhibited different mean values and variability. Unless corrected, these biases would have hindered the exploitation of the useful information they contained during data assimilation. In order to allow assimilation to proceed, the satellite *SWI* observations were rescaled into the space of the model open loop ensemble *SWI* mean values. The rescaling was performed using the cumulative distribution function (CDF) matching technique of Reichle and Koster (2004) applied to a subset of the data, with matching being performed over both space and time.

The assimilation also requires estimation of the observation error variances. The triple collocation (TC) approach was used for this step (Stoffelen 1998: Draper et al. 2013). TC enables the observation errors to be estimated provided that a triplet of independent unbiased datasets is available, one of which (in this case the model open loop dataset) is chosen as a reference. The triplet used here consisted of the model open loop ensemble mean, the ASAR and the ASCAT *SWI* values.

TC is based on the use of N sets of measurements with each set containing a measurement from each of three data sources taken at the same position. Often in TC studies the different samples are acquired at different instances in time. However, Zwieback et al. (2012) point out that the method can be applied to data distributed in space as well as time. This approach was adopted here due to the limited number of ASAR scenes available. Typically N should be large to obtain accurate estimates of the *SWI* error variances. Zwieback et al. (2012) calculate that 100 samples are needed to produce a standard deviation of the *SWI* error variance of 0.22, and that if a relative accuracy of 0.1 is needed 500 samples are

required. The method requires that there should be no correlations between TC errors across space or time. To reduce temporal correlations between errors, the original image set of 20 ASAR *SWI* images in 2007 and 2008 was thinned to 14, so that the average time difference between adjacent images was about 23 days. The spatial thinning applied to the samples within each image resulted in approximately 16 samples being selected per image with an average separation distance of about 40 km, with the result that adjacent samples were generally based upon different ASCAT 12.5 km pixels. Spatial thinning was applied to each image independently, so that successive images were unlikely to provide samples at the same spatial positions. The total number (N) of samples used in the TC analysis was 233. Zwieback et al. (2012) show that the error on the i'th *SWI* error variance σ_i (assuming that the error noise is normally distributed) can be calculated using –

$$\mathrm{Var}(\sigma_i) = (2\,\sigma^2_i + \sigma_i\,\sigma_j + \sigma_i\,\sigma_k + \sigma_j\,\sigma_k)/N \qquad (2)$$

where i, j, k represent data sources 1,2 and 3.

A potential pitfall of the TC method applied here is that ASAR and ASCAT are both active sensors measuring backscatter coefficients, and as a result their *SWI* error values may not be independent in spite of the great difference between their resolutions. However, the correlation between the errors was found to be close to zero, as required by the TC analysis. In addition, the correlation between the model open loop mean *SWI* errors and the ASAR *SWI* errors was very small, as was the corresponding correlation between the model and ASCAT *SWI* errors. This justified the assumption of uncorrelated observation errors made in the data assimilation scheme.

Table 4 gives the *SWI* error variances for model, ASAR and ASCAT in the model state space, together with their standard deviations. It is apparent that the ASAR error variance is less than that of the model, and that the same is true for the ASCAT error variance. The ASCAT error variance is significantly higher than that for ASAR, though it must be remembered that the ASCAT data are not disaggregated. The TC analysis also did not take into account the fact that the ASCAT *SWI* retrievals were of lower resolution than those of the model and ASAR, so that the ASCAT *SWI* error variance will contain a component due to representativeness error.

Table 4. *SWI* error variances from triple collocation.

***SWI* data type**	***SWI* error variance**	**Standard deviation of *SWI* error variance**
Model	0.16	0.02
ASAR	0.06	0.01
ASCAT	0.12	0.02

2.2.4 Data assimilation scheme

The method of assimilation employed was a local Ensemble Transform Kalman Filter. A detailed description of the filter is given in Garcia-Pintado et al. (2015), where it was used, in conjunction with a Shallow Water Equation model for inundation forecasting, to assimilate satellite-based water levels, with HSPF being used for generating the runoff ensemble inflow into the flood domain. Here, the assimilation was conducted at the time of a satellite overpass, so that the hydrologic model simulations were sequentially interrupted.

As noted in Garcia-Pintado et al. (2015), "the Ensemble Kalman Filter (EnKF), introduced in Evensen (1994), is characterized by a two-step feedback loop: a prediction followed by an observation-based state update. In the prediction phase, each individual ensemble member is evolved forward in time by the forecast model until the time of the next observation. This means that the model state variables are forecast by the hydrologic model with appropriate forecast boundary conditions. At the time of an observation (i.e. at image acquisition time), the ensemble Kalman filter equations are used to update the ensemble (Evensen 1994). This update may be thought of as a linear combination of the forecast and the observations, weighted by the relative uncertainties in the model and observation data. The weights involved are contained within the Kalman gain matrix **K.**" An ensemble size of 50 members was used. The perturbation factors used to perturb the rainfall have been described in section 2.2.1.1. The ensemble spread appeared reasonable when examined visually.

Typically the number of ensemble members is much smaller than the dimension of the state vector, leading to under-sampling. This is the case here, as, because the hydrologic model is distributed, the state vector contains $\sim 10^5$ elements. Undersampling often manifests itself as spurious (unphysical) forecast error correlations, which contribute to significant increments updating the state at locations further from the location of the observation than is plausible (Petrie and Dance 2010). Localization techniques are often used to ameliorate the problem. In this study, localization was performed using a domain localization method (Ott et al. 2004; Hunt et al. 2007), whereby assimilation is applied independently to a series of disjoint local domains in physical space. For each local assimilation, only observations within some defined cut-off radius are considered. Furthermore, the weight of observations is reduced as a function of their distance from the local analysis domain by increasing their assumed error variance. To account for the fact that the data had been thinned, the observation weighting function used in the localization procedure was given a relative large spatial correlation length of 150 km (see Garcia-Pintado et al. (2015)).

Table 2 describes the topHSPF distributed state variables (see Bicknell et al. 1997), which evolved in space and time as the assimilation proceeded. All state variables in Table 2 were updated by the assimilation analysis, so they were provided as (spatially varying) initial conditions for each model ensemble member run.

In addition to filter localization, we inflated the analysis variance after each assimilation step to support the long-term stability of the data assimilation itself. The inflation was such that the analysis variance matched the background variance. This inflation strategy is a conservative one to avoid filter divergence (Jazwinski 1970). For comparison, a standard rule-of-thumb in oceanography and meteorology is to estimate unknown error covariances conservatively (e.g. Cohn 2008).

In the assimilation of the ASCAT data, note that the coarser-resolution ASCAT measurements were re-sampled onto a 1 km grid and assimilated as if they were 1 km resolution observations. This had the advantage that an innovation was calculated between a 1 km ASCAT *SWI* and 1 km model *SWI,* and used to modify the latter directly. This gave an ASCAT assimilation a better chance of matching the equivalent ASAR assimilation, because the same model *SWI* value was used to construct both innovations. However, this approach could cause a problem because the assimilation could use the (overly smooth) ASCAT observations to dampen all 1 km scale variability predicted by the model. The "smoothness" of the 1 km ASCAT observations is not a reflection of reality but an artefact of the inadequate spatial resolution of the ASCAT observations themselves. A solution could be to keep the ASCAT observations at their native spatial resolution in the assimilation, and add a spatial aggregator to the observation operator to aggregate the 1 km model state variables to match the coarser-resolution ASCAT soil moisture retrievals. This would not spuriously remove 1 km variability generated by the model. However, in this case, because of the computing limitation on assimilation, we assimilated on average less than one 1 km *SWI* pixel per 12.5 km ASCAT pixel, resulting in at most 1 innovation per ASCAT pixel. Thus any variations at 1 km scale in the model should largely remain after the assimilation.

2.2.5 Performance measurement

The performance of the data assimilation was assessed by comparing the observed and modelled discharge using a number of statistical scores. These included the Nash-Sutcliffe (NS) efficiency index (Nash and Sutcliffe 1970), the Efficiency (Eff) of assimilation (Massari et al. 2015) and the Normalized Error Reduction (NER) (Chen et al. 2011). NS produces a result in the range [-∞, 1], with a value of 1 corresponding to a perfect model. Eff is an estimate of the percentage of improvement (Eff > 0) or deterioration (Eff < 0) as a result of the assimilation, and lies in the range -∞ to 100. It compares the variance of the differences between the open loop and observed flows with the variance of the differences between the flows corrected by assimilation and observed flows, according to equation (13) of Massari et al. (2015). NER is a dimensionless value estimating the percentage reduction (or increase) of root mean square error (RMSE) between the modelled and observed discharge as a result of the assimilation. NER again ranges between -∞ to 100, and the higher the NER value, the higher the RMSE reduction. These scores were calculated for each year, for the period between the first and last assimilation times in the year.

3 Results

Figs. 3 - 5 show the comparisons as a function of time between the mean modelled runoff using data assimilation, the mean open loop model runoff, and the observed runoff, for ASAR and ASCAT *SWI* images for May-October during 2007 and 2008, for the three main rivers in the catchment, namely the Severn at Bewdley, the Avon at Evesham, and the Teme at Knightsford Bridge respectively. The results for ASAR and ASCAT are summarized in table 5.

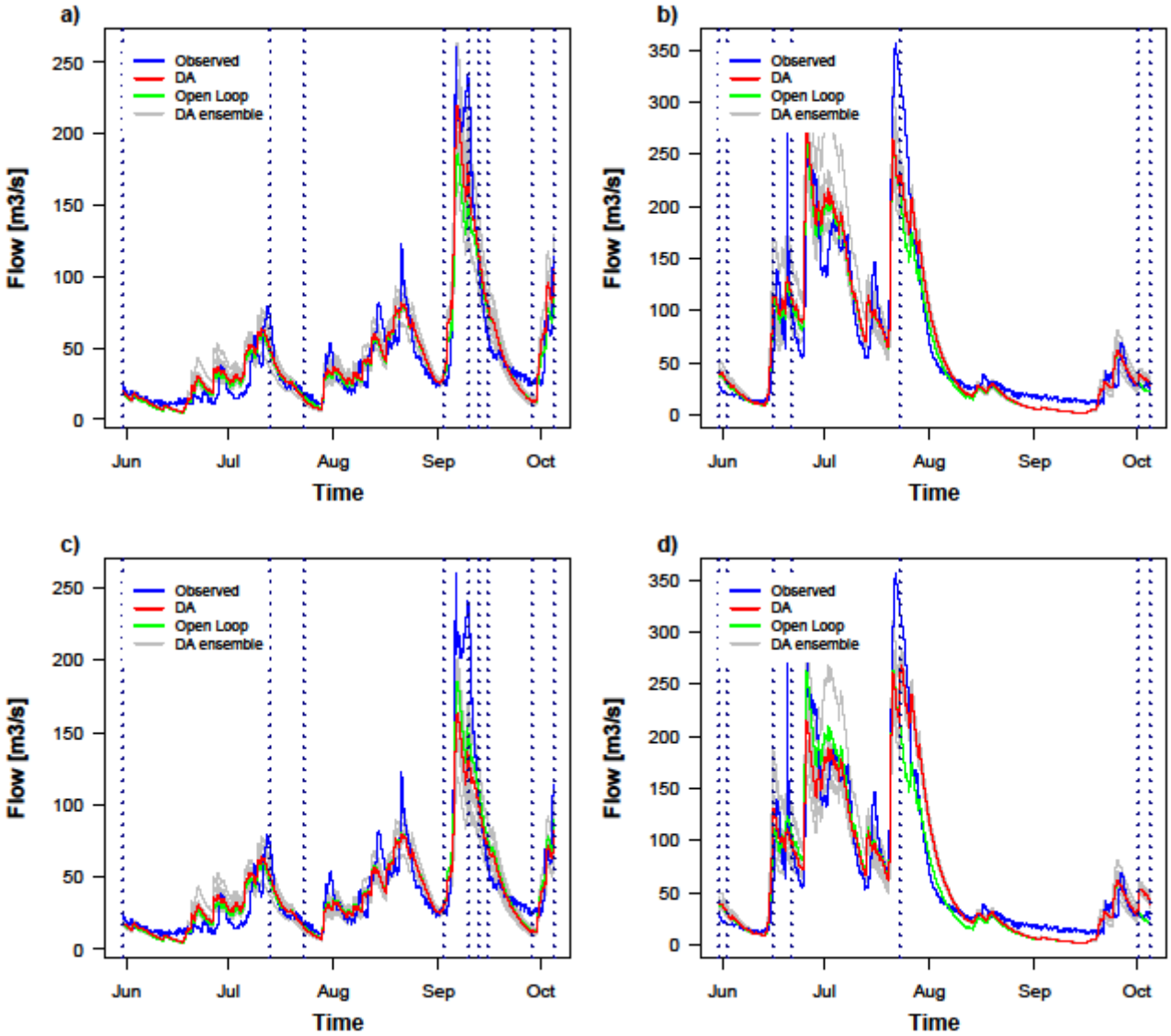

Figure 3. Runoff results for assimilation of satellite SWI data for 2007-8 for Severn at Bewdley: (a) ASAR assimilation for 2008, (b) ASAR assimilation for 2007, (c) ASCAT assimilation for 2008, and (d) ASCAT assimilation for 2007 (vertical dashed lines indicate satellite overpass times).

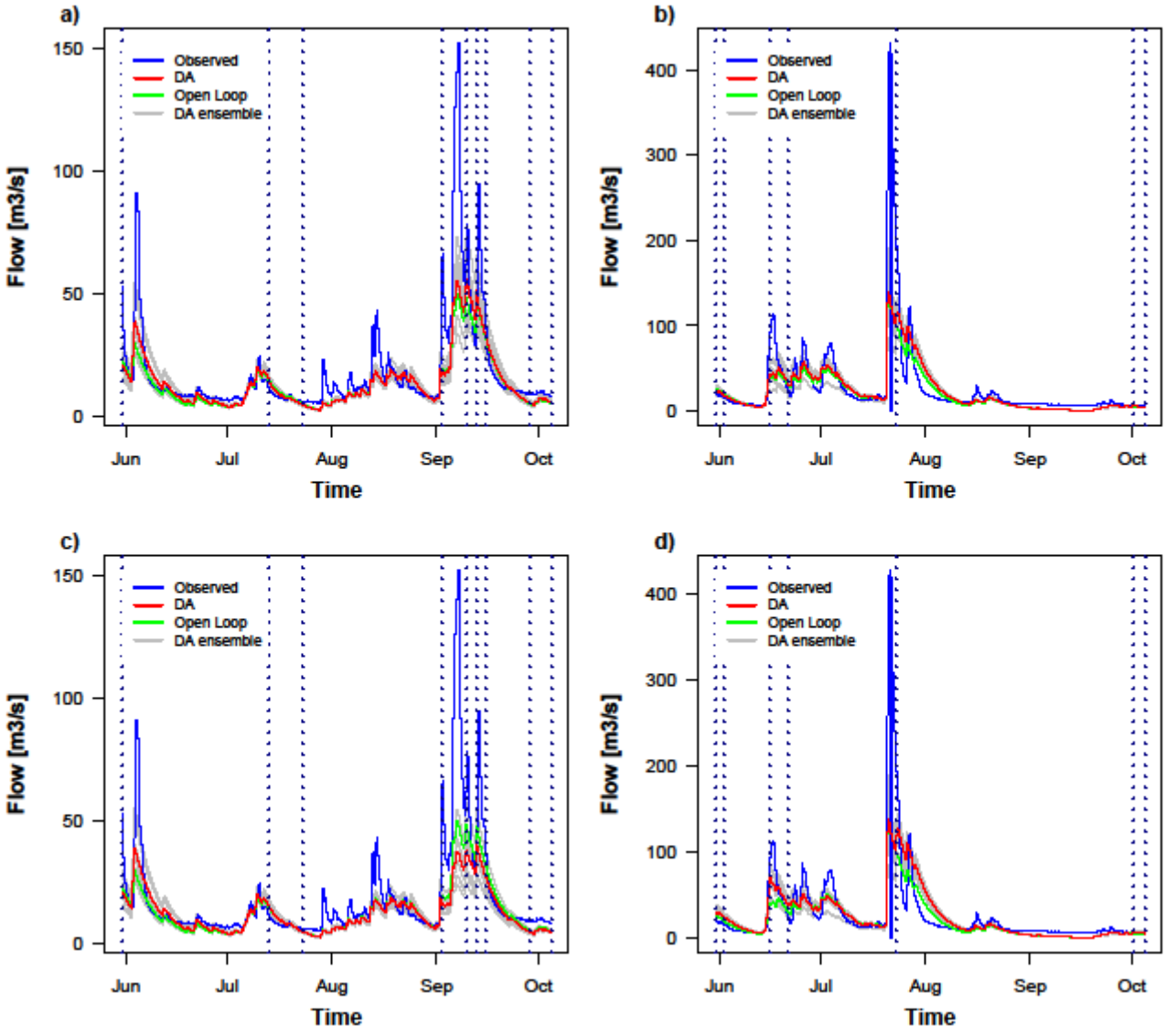

Figure 4. Runoff results for assimilation of satellite SWI data for 2007-8 for Avon at Evesham: (a) ASAR assimilation for 2008, (b) ASAR assimilation for 2007, (c) ASCAT assimilation for 2008, and (d) ASCAT assimilation for 2007 (vertical dashed lines indicate satellite overpass times).

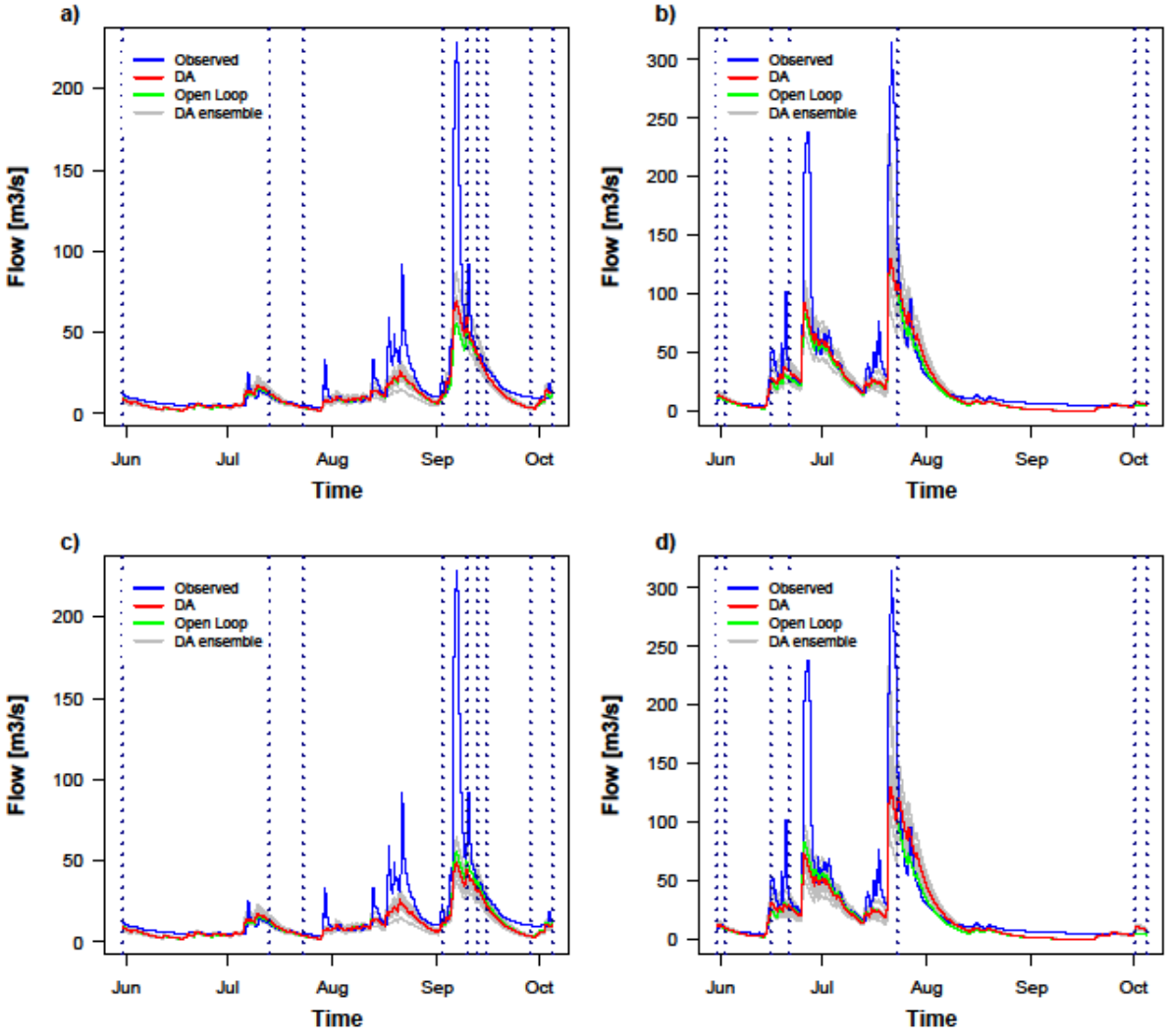

Figure 5. Runoff results for assimilation of satellite SWI data for 2007-8 for Teme at Knightsford Bridge: (a) ASAR assimilation for 2008, (b) ASAR assimilation for 2007, (c) ASCAT assimilation for 2008, and (d) ASCAT assimilation for 2007 (vertical dashed lines indicate satellite overpass times).

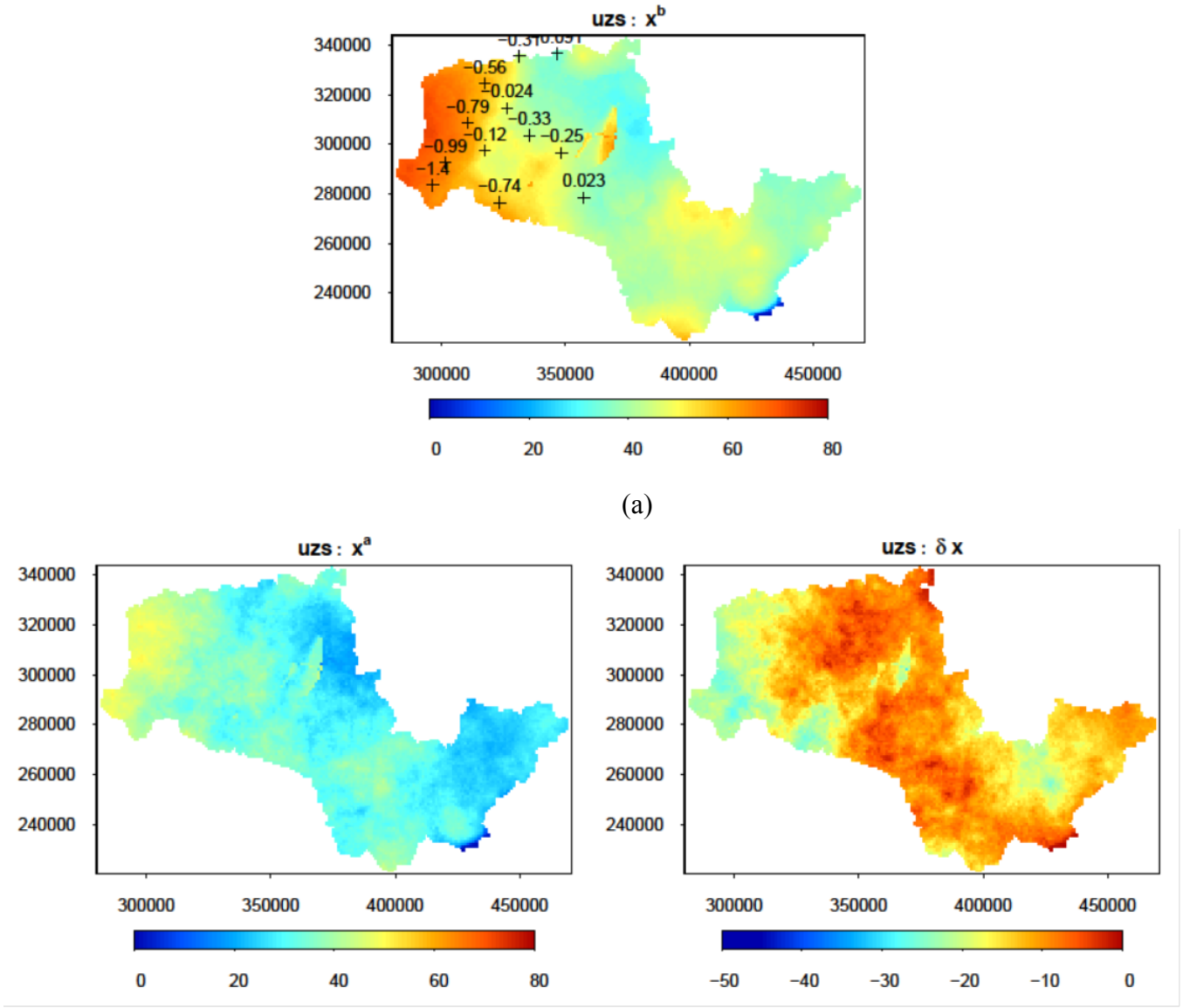

Figure 6. (a) Spatial distribution of upper zone storage uzs prior the ASAR assimilation of 13/Jun/2008 (crosses mark positions of SWI values assimilated, and corresponding figures indicate resulting changes in uzs at those positions; observations limited to western domain in this example due to satellite swaths), (b) updated uzs distribution after assimilation, and (c) changes in uzs as a result of the assimilation.

Table 5. Summary of results for ASAR and ASCAT *SWI* image assimilation (ASCAT results in brackets).

River	Year	Mean change in upper zone storage (*uzs*)	Nash-Sutcliffe efficiency (DA)	Nash-Sutcliffe efficiency (Open Loop)	Efficiency Eff (%)	Normalized Error Reduction NER (%)
Severn	2008	2.3 (0.26)	0.87 (0.78)	0.83	23.8 (-34.1)	12.7 (-15.8)
	2007	5.3 (6.6)	0.87 (0.87)	0.86	6.3 (2.2)	3.2 (1.1)
Avon	2008	2.3 (0.3)	0.57 (0.41)	0.51	12.0 (-21.4)	6.2 (-10.2)
	2007	5.3 (6.6)	0.58 (0.58)	0.59	-1.0 (-1.4)	-0.4 (-0.7)
Teme	2008	2.3 (0.3)	0.53 (0.38)	0.44	16.5 (-10.3)	8.6 (-5.0)
	2007	5.3 (6.6)	0.63 (0.57)	0.61	5.8 (-8.2)	3.0 (-4.0)

In fig. 3a, for the Severn at Bewdley in 2008, the assimilation forced the modelled flow closer to the observed flow for all the assimilations (including the flood period during September 2008), and the Eff value was 23.8%, so that the assimilation of ASAR *SWI* images definitely assisted the model. This was in spite of the fact that the model was relatively well-calibrated, with initial good agreement between the model Open Loop and observed flows (the NS Open Loop efficiency was 0.83), so that there was limited opportunity for the assimilation to produce improvements. It is likely that the improvement would have increased if it had been possible to obtain ASAR data more frequently (e.g. at the Sentinel-1 revisit frequency), as on average only about one suitable ASAR scene could be obtained each month.

However, the results for ASCAT in 2008 (fig. 3c) were worse than those for ASAR, giving an Eff value of -34.1%, so that the assimilation was hindering rather than helping during this period. In this case, it appears that the higher resolution of ASAR data did increase efficiency compared to ASCAT data that were not disaggregated and limited to the temporal frequency of ASAR.

The results for the Severn at Bewdley in 2007 (fig. 3b) were dominated by those due to the flood events that occurred in June and July 2007, with the July flood being a 1-in-150-year event. The Eff value was 6.3%, indicating that the assimilation had had little effect (though this was still positive). It is likely that this was because, as stated by Crow and Ryu (2009), "for very intense rainfall events, antecedent SM conditions may be of minor importance as the infiltration excess overland flow mechanism is dominant and rainfall runs off before it has the opportunity to infiltrate." From the point of view of the assimilation, both model and observed *SWI* values would have close to unity, and their differences would have been small, making innovations small also.

This argument is borne out by the results for ASCAT for 2007 (fig. 3d), which show a similar behavior to those for ASAR, with again a low Eff value of 2.2%. It appears that the remotely sensed *SWI* data, irrespective of whether from ASCAT or ASAR, were of minor importance during this extreme flood period.

Similar behavior to the above was exhibited by the other two rivers, the Avon and Teme, in figs. 4 and 5 respectively.

Fig. 6 illustrates the distributed nature of the hydrologic model, and shows the spatial distribution of *uzs* before and after the ASAR assimilation of 13/Jun/2008 (i.e. the background and analysis *uzs* maps), together with the resulting changes in *uzs*. Changes in *lzs* and *agws* for this assimilation followed a similar pattern to those for *uzs*.

As stated above, the model was relatively well-calibrated, so that in the cases examined there was limited opportunity for the assimilation to produce improvements. The study has used the observed precipitation to drive the hydrologic model in a hindcasting mode. The interpolated precipitation fields were obtained from point rain-gauge measurements that may well have missed some convective rain cells, and in addition stochastic error fields were added to precipitation inputs. Nevertheless, the errors in the precipitation from a Numerical Weather Prediction (NWP) model are likely to be larger in the quantity, position and timing of the rainfall in a real forecast situation than those of observed precipitation (see e.g. Lewis et al. 2015). It would have been possible to use the system to test whether the assimilation was more effective in a situation where the precipitation errors and biases were larger. However, the magnitude of the errors and biases on NWP forecast precipitation is still an open research question

(Mittermaier et al. 2013), and as such it was felt that to explore this route would have been too speculative.

4 Discussion

The study has compared the assimilation of ASAR *SWI* data to that of ASCAT *SWI* data obtained at the same time. It is freely acknowledged that this approach biases against ASCAT data because ASAR data, while having high spatial resolution, have only low temporal resolution, whereas ASCAT data can be obtained virtually every day. The approach has been adopted on the premise that, in future SM studies of this kind, ASAR data would be replaced with Sentinel-1 data having both high temporal and high spatial resolution. Cenci et al. (2016b) compared the assimilation of Sentinel-1A *SWI* data with disaggregated ASCAT H08 data using a simple nudging scheme in conjunction with a distributed model. The authors found that Sentinel-1A data only marginally improved discharge simulations, whereas ASCAT data showed similar but more marked trends, arguably due to their higher temporal resolution. Further improvements are expected when both Sentinel-1A and B data are assimilated. Similarly, Azimi et al. (2020) assimilated the SCATSAR-*SWI* product into the SWAT hydrological model and found an improvement in discharge simulation, though the majority of this appeared to be due to the higher temporal frequency of ASCAT.

The model parameters for topHSPF were estimated by calibration, and further research also needs to be carried out to ascertain whether it is possible for the assimilation system to estimate these at the same time as the model state variables. A feature of the assimilation scheme is that, if necessary, uncertain parameters in topHSPF can be simultaneously estimated with the model state at the time of the assimilation by augmenting the model state vector with these model parameters (Smith et al. 2011; Smith et al. 2013; Garcia-Pintado et al. 2013). An advantage of this approach is that the assimilation scheme has the potential to be able to take into account correlations between errors in the parameters and errors in the model variables.

A method for the production of 1 km Sentinel-1 surface moisture data on a global scale, in the form of an *SWI* product suitable for hydrological studies, has recently been developed by Bauer-Marschallinger et al. (2019). It is intended that this data should be one of the products of the Copernicus Global Land Service (Wagner et al. 2016). A dynamic Gaussian upscaling technique is used for upscaling of 10 m Sentinel-1 imagery to 1 km, and land cover classes that do not lend themselves to meaningful retrieval of surface SM (e.g. urban, water) are masked out (Hornacek et al. 2012). This method is not the same as that employed in this study, where only 75 m ASAR surface SM measurements over grassland are agglomerated within each 1 km pixel. It would be interesting to compare the results of assimilating Sentinel-1 *SWI* data obtained in a similar manner over grassland to those obtained with Sentinel-1 using the method developed by Bauer-Marschallinger et al. (2019).

5 Conclusion

The study has investigated whether the assimilation of high resolution remotely sensed SM data into a distributed hydrologic model is able to improve runoff prediction, in the case where the SM data are used in conjunction with a land cover map. The advantages of the approach include the ability to reduce contamination of the surface soil signal due to vegetation, radar artefacts, pixels containing more than one land cover type and land cover classes not providing meaningful soil moistures. ASAR SM values

were obtained over pixels of low vegetation coverage (grassland), requiring that at least 50% of the 75 m ASAR pixels in each 1 km cell of the hydrologic model coincided with grassland. The signal-to-noise ratios of the ASAR SM values were further increased using an adaptive thinning algorithm. A spatially distributed version of the hydrologic model HSPF was developed to enable high resolution surface SM information to be ingested. In a triple collocation analysis, the ASAR *SWI* error variance estimated was less than those of both the model and the ASCAT data, though the ASCAT data were not disaggregated and the ASCAT temporal sampling frequency was artificially limited.

Results for 2008 showed that the assimilation of ASAR *SWI* values improved the predicted runoff for all images. The improvement was less marked for 2007, probably because the antecedent SM conditions were of reduced importance during extreme flooding. However, in a typical year, conditions would generally be more similar to those for 2008 than 2007. Particularly for 2008, the higher resolution of ASAR data did increase efficiencies compared to ASCAT data that were not disaggregated and limited to the temporal frequency of ASAR. These results are based on a limited set of validation data, and future work will seek to extend this, as well as assimilating a denser set of observations. However, this work will use Sentinel-1 rather than ASAR data, because the method is likely to give better results with a Sentinel-1-based product (e.g. SCATSAR-*SWI* (Bauer-Marschallinger et al. 2018)) due to its high temporal resolution. The results illustrate the potential importance of assimilating soil moisture from high resolution SARs for operational flow forecasting.

Acknowledgements

This work was funded under the UK Natural Environment Research Council Flooding from Intense Rainfall SINATRA project (NE/K00896X/1).

References

Albergel, C., C. Rudiger, T. Pellarin, J.C. Calvet, N. Fritz, F. Froissard, D. Suquia, A. Petitpa, B. Piguet and E. Martin, 2008: From near-surface to root zone soil moisture using an exponential filter: an assessment of the method based on in situ observations and model simulations. *Hydrology and Earth System Sciences*, **12**(6), 1323-1337.

Aubert, M., N.N. Baghdadi, M. Zribi, K. Ose, M. El Hajj, E. Vaudour and E. Gonzalez-Sosa, 2013: Towards an operational bare soil moisture mapping using TeraSAR-X data acquired over agricultural areas. *IEEE JSTARS*, **6** (2), 900-915.

Azimi, S., A.B. Dariane, S. Modanesi, B. Bauer-Marschallinger, R. Bindlish, W. Wagner, C. Massari, 2020: Assimilation of Sentinel 1 and SMAP - based satellite soil moisture retrievals into SWAT hydrological model: the impact of satellite revisit time and product spatial resolution on flood simulations in small basins. J. Hydrology, **581**, 124367.

Barrett, B.W., E. Dwyer, P. Whelan, 2009: Soil moisture retrieval from active spaceborne microwave observations: an evaluation of current techniques. *Remote Sensing* **1**(3), 210-242.

Bauer-Marschallinger, B., C. Paulik, S. Hochstoger, T. Mistelbauer, S. Modanesi, L. Ciabatti, C. Massari, L. Brocca and W. Wagner, 2018: Soil moisture from fusion of scatterometer and SAR: Closing the scale gap with temporal filtering. *Remote Sensing*, **10**, 1030.

Bauer-Marschallinger, B., V. Freeman, S. Cao, C. Paulik, S. Schaufler, T. Stachl, S. Modanesi, C. Massari, L. Ciabatta, L. Brocca, W. Wagner, 2019: Towards global soil moisture monitoring with Sentinel-1: harnessing assets and overcoming obstacles. *IEEE Trans. Geoscience and Remote Sensing*, **57**(1), 520-9.

Bicknell, B.R., J.C. Imhoff, J.L. Kittle, A.S. Donigian and R.C. Johanson, 1997: Hydrological Simulation Program - Fortran, User's manual for version 11. U.S. Environmental Protection Agency, National Exposure Research Laboratory, Athens, Ga., EPA/600/R-97/080, 755 p.

Blenkinsop, S., E. Lewis, S.C. Chan and H.J. Fowler, 2017: Quality-control of an hourly rainfall dataset and climatology of extremes for the UK. *Int. J. Climatology*, **37**(2), 722-740. doi:10/1002/joc.4735.

Brocca, L., T. Moramarco, F. Melone, W. Wagner, S. Hasenauer and S. Hahn, 2012a: Assimilation of surface- and root-zone ASCAT soil moisture products into rainfall-runoff modelling. *IEEE. Trans. GeoScience and Remote Sensing*, **50**(7), 2542-2555.

Brocca, L., F. Melone, T. Moramarco, G. Zucco and W. Wagner, 2012b: Soil moisture assimilation into rainfall-runoff modelling: which is the impact of the model structure on runoff predictions? *Geophysical Research Abstracts*, **14**, EGU2012-2299.

Cenci, L., P. Laiolo, S. Gabellani, L. Campo, F. Silvestro, F. Delogu, G. Boni and R. Rudari, 2016a. Assimilation of H-SAF Soil Moisture Products for Flash Flood Early Warning Systems. Case Study: Mediterranean Catchments. *IEEE JSTARS*, **9**(12), 5634-5646. doi: 10.1109/JSTARS.2016.2598475.

Cenci, L., G.B. Pulvirenti, M. Chini, P. Matgen, S. Gabellani, L. Campo, F. Silvestro, C. Versaci, P. Campanella and L. Candela, 2016b: Satellite soil moisture assimilation: preliminary assessment of the Sentinel 1 potentialities. *Proc. IGARSS*, Beijing, July 10-15, 2016, 3098-3101.

Chen, F., W.T. Crow, P.J. Starks and D.N. Moriasi, 2011: Improving hydrologic predictions of a catchment model via assimilation of surface soil moisture. *Advances in Water Resources*, **34**(4), 526-536. Doi: 10.1016/j.advwatres.2011.01.011.

Cohn, S, 2008: An Introduction to Estimation Theory (Special Issue in Data Assimilation in Meteorology and Oceanography: Theory and Practice). *Journal of the Meteorological Society of Japan.* Ser. II. DOI:10.2151/jmsj1965.75.1B_257.

Corato, G., P. Matgen, F. Fenicia, S. Schlaffer and M. Chini, 2014: Assimilating satellite-derived soil moisture products into a distributed hydrological model. *Proc. IEEE Int. Symp. Geosci. Rem. Sens.,* doi: 10.1109/IGARSS.2014.6947189.

Crow, W.T. and D. Ryu, 2009: A new data assimilation approach for improving runoff prediction using remotely-sensed soil moisture retrievals. *Hydrology and Earth System Sciences*, **13**, 1-16.

Donigian Jr. A.S., B.R. Bicknell and J.C. Imhoff, 1995: Hydrological Simulation Program—FORTRAN (HSPF). In: Singh, V.P., Ed., Computer Models of Watershed Hydrology, Water Resources Pubs, Highlands Ranch, 395-442.

Dostalova, A., M. Boubkova, D. Sabel, B. Bauer-Marschallinger and W. Wagner, 2014: Seven Years of Advanced Synthetic Aperture Radar (ASAR) Global Monitoring (GM) of Surface Soil Moisture over Africa. *Remote Sensing*, **6**(8), 7683-7707.

Draper, C., R. Reichle, R. Jeu, V. Naeimi, R. Parinussa and W. Wagner, 2013: Estimating root mean square errors in remotely sensed soil moisture over continental scale domains. *Remote Sensing of Environment*, **137**, 288-298.

Evensen, G, 1994: Sequential data assimilation with a nonlinear quasi-geostrophic model using Monte Carlo methods to forecast error statistics. *Journal of Geophysical Research*, **99**, 10143-10162. URl: http://dx.doi.org/10.1029/94J00572.

Evensen, G, 2004: Sampling strategies and square root analysis schemes for the EnKF. *Ocean Dynamics*, **54**(6), 539-560.

Francois, C., A. Quesney and C. Ottle, 2003: Sequential assimilation of ERS-1 SAR data coupled land surface-hydrological model using an extended Kalman Filter. *Journal of Hydrometeorology,* **4**(2), 473-487.

Garcia-Pintado, J., J.C. Neal, D.C. Mason, S.L. Dance and P.D. Bates, 2013: Scheduling satellite-based SAR acquisition for sequential assimilation of water level observations into flood modelling. *Journal of Hydrology*, **495**, pp 252-266, doi: 10.1016/j.jhydrol.2013.03.050.

Garcia-Pintado, J., D.C. Mason, S.L. Dance, H.L. Cloke, J.C. Neal, J. Freer and P.D. Bates, 2015: Satellite-supported flood forecast in river networks: a real case study. *Journal of Hydrology,* **523**, 706-724. doi: 10.1016/j.hydrol.2015.01.084.

Greifeneder, F., C. Notarnicola, G. Cuozzo, N. Spindler, G. Bertoldi, S. Della Chiesa, G. Niedrist, J. Stamenkovic and W. Wagner, 2014: Analysis of ASAR Wide Swath Mode time series for the retrieval of soil moisture in mountainous areas. *Geophysical Research Abstracts*, **16**, EGU2014-14383.

Gruber, A., W. Wagner, A. Hegyiova, F. Greifeneder and S. Schlaffer, 2013: Potential of Sentinel-1 for high-resolution soil moisture monitoring. *Proc. IEEE Int. Symp. Geosci. Rem. Sens.*, 4030-4033. doi: 10.1109/IGARSS.2013.6723717.

Hall, D.K., G.A. Riggs, V.V. Salomonson, N.E. Di Girolamo and K.J. Bayr, 2002: MODIS snow-cover products. *Remote Sensing of Environment*, **83**, 181-194.

H-SAF, 2015: Product User Manual for product H08 – SM-OBS-2 (Small-scale surface soil moisture by radar scatterometer). Doc. No: SAF/HSAF/PUM-08. 29 pages.

Hornacek, M., W. Wagner, D. Sabel, H-L. Truong, P. Snoeij, T. Hahmann, E. Diedrich and M. Doubkova, 2012: Potential for high resolution systematic global surface soil moisture retrieval via change detection using Sentinel-1. *IEEE JSTARS*, **5**(4), 1303-1311.

Hough, M.N. and R.J.A. Jones, 1997: The United Kingdom Meteorological Office rainfall and evaporation calculation system: MORECS version 2.0-an overview. *Hydrology and Earth System Sciences*, **1**, 227-239, http://doi.org/10.5194/hess-1-227-1997.

Hunt, B.R., E.J. Kostelich and I. Szunyogh, 2007: Efficient data assimilation for spatiotemporal chaos: a local ensemble transform Kalman filter. *Physica D; Nonlinear Phenomena* **230**, 112-126.

Jackson, T.J., T.J. Schmugge, A.D. Nicks, G.A. Coleman and E.T. Engman, 1981: Soil-moisture updating and microwave remote-sensing for hydrological simulation. *Hydrological Sciences Bulletin*, **26**(3), 303-319, doi: 10.1080/02626668109490889.

Jazwinski, A.H, 1970: Stochastic Processes and Filtering Theory. Academic Press, 376pp.

Kong, X. and S.R. Dorling, 2008: Near-surface soil moisture retrieval from ASAR WSM imagery using a principal component analysis. *International Journal of Remote Sensing* **29**(10), 2925-2942.

Lacava, T., P. Matgen, L. Brocca, M. Bittelli, N. Pergola, T. Moramarco and V. Tramutoli, 2012: A first assessment of the SMOS soil moisture product with in situ and modelled data in Italy and Luxembourg. *IEEE. Trans. GeoScience and Remote Sening.,* **50**(5), 1612-1622.

Lewis, H., M. Mittermaier, K. Mylne, K. Norman et al., 2015: From months to minutes – exploring the high-resolution rainfall observation and prediction during the UK winter storms of 2013/2014. *Meteorological Applications*, **22**, 90-104.

Loew, A., R. Ludwig and W. Mauser, 2006: Derivation of surface soil moisture from ENVISAT ASAR WS and image mode data in agricultural areas. *IEEE Trans. GeoScience and Remote Sensing,* **44**(4), 889-899.

Mason, D.C., J. Garcia-Pintado, H.L. Cloke and S.L. Dance, 2016: Evidence of a topographic signal in surface soil moisture derived from ENVISAT ASAR Wide Swath data. *International Journal of Applied Earth Observation and Geoinformation.* **45B**, 178-186, doi: 10.1016/j.jag.2015.02.004.

Massari, C., L. Brocca, A. Tarpanelli and T. Moramarco, 2015: Data Assimilation of Satellite Soil Moisture into Rainfall-Runoff Modelling: A Complex Recipe? *Remote Sensing*, *7*, 11403-11433; doi:10.3390/rs70911403.

Mittermaier, M., N. Roberts and S.A. Thompson, 2013: A long-term assessment of precipitation forecast skill using the Fractions Skill Score. *Meteorological Applications*, **20**, 176-186.

Morton, D., C. Rowland, C. Wood, L. Meek, C. Marston, G. Smith, R. Wadsworth and I.C. Simpson, 2011: Final Report for LCM2007 – the new UK Land Cover Map. CS Technical Report No 11/07. Centre for Ecology & Hydrology. Natural Environment Research Council.

Naeimi, V., K. Scipal, Z. Bartalis, S. Hasenauer and W. Wagner. 2009: An improved soil moisture retrieval algorithm for ERS and MetOp scatterometer observations. *IEEE Trans. GeoScience and Remote Sensing*, **47**(7), 1999-2013, doi:10.1109/TGRS.2008.2011617.

Nash, J.E. and J.V. Sutcliffe, 1970: River flow forecasting through conceptual models part I – A discussion of principles. *Journal of Hydrology*, **10**(3), 282-290.

Neal, J., G.J-P. Schumann and P.D. Bates, 2012: A sub-grid channel model for simulating river hydraulics and floodplain inundation over large and data sparse areas. *Water Resources Research*, **48**, doi: 10.1029/2012WR012514.

Ochotta, T., C. Gebhardt, D. Saupe and W. Wergen, 2005: Adaptive thinning of atmospheric observations in data assimilation with vector quantization and filtering methods. *Quarterly Journal of Royal Meteorological Society*, **131**, 3427-3427.

Ott, E., B. Hunt, I. Szunyogh, A. Zimin, E. Kostelich, M. Corazza, E. Kalnay, D. Patil and J. Yorke, 2004: A local ensemble Kalman filter for atmospheric data assimilation. *Tellus A*, 56. URL: http://www.tellusa.net/index.php/tellusa/article/view/14462.

Parajka, J., V. Naeimi, G. Bloeschl, W. Wagner, R. Merz and K. Scipal, 2005: Assimilating scatterometer soil moisture data into conceptual hydrologic models at the regional scale. *Hydrology and Earth System Sciences*, **10**, 353-368.

Parrens, M., E. Zakharova, S. Lafont, J-C. Calvet, Y. Kerr, W. Wagner and J-P. Wigneron, 2012: Comparing soil moisture retrievals from SMOS and ASCAT over France. *Hydrology and Earth System Sciences,* **16**, 423-440.

Pathe, C., W. Wagner, D. Sabel, M. Doubkova and J.B. Basara, 2009: Using ENVISAT ASAR global mode data for surface soil moisture retrieval over Oklahoma, USA. *IEEE Trans. GeoScience and Remote Sensing,* **47**(2), 468-480.

Pauwels, V.R.N., A. Balenzano, G. Satalino, H. Skriver, N.E.C. Verhoest and F. Mattia, 2009: Optimization of soil moisture model parameters using Synthetic Aperture Radar data: an integrated multidisciplinary approach. *IEEE Trans. GeoScience and Remote Sensing*, 47(2) 455-467.

Petrie, R.E. and S.L. Dance, 2010: Ensemble-based data assimilation and the localization problem. *Weather,* **65**, 3, pp65-69, doi:10.1002/wea.505.

Plaza, D.A., R. De Keyser, G.J.M. De Lannoy, L. Giustarini, P. Matgen and V.R.N. Pauwels, 2012: The importance of parameter resampling for soil moisture data assimilation into hydrologic models using the particle filter. *Hydrology and Earth System Sciences*, **16**(2), 375-390. doi: 10.5194/hess-16-375-2012.

Pratola, C., B. Barrett, A. Gruber, G. Kiely and E. Dwyer, 2014: Evaluation of a Global Soil Moisture Product from Finer Spatial Resolution SAR Data and Ground Measurements at Irish Sites. *Remote Sensing*, **6**(9), 8190-8219.

Reichle, R.H. and R.D. Koster, 2004: Bias reduction in short records of satellite soil moisture. *Geophysical Research Letters*, **331**(9), Lo19501.

Seneviratne, S.L., T. Corti, E.L. Davin, M. Hirschi, E.B. Jaeger, I. Lehner, B. Orlowsky and A.J. Teuling, 2010: Investigating soil moisture–climate interactions in a changing climate: A review. *Earth Science Reviews* **99**(3/4), 125-161.

Smith, P.J., S.L. Dance and N.K. Nichols, 2011: A hybrid data assimilation scheme for model parameter estimation: application to morphodynamic modelling. *Computers and Fluids,* **46**, pp 436-441, doi:10.1016/j.compfluid.2011.01.010.

Smith, P.J., G.D. Thornhill, S.L. Dance, A.S. Lawless, D.C. Mason and N.K. Nichols, 2013: Data assimilation for state and parameter estimation: application to morphodynamic modelling. *Quarterly Journal of Royal Meteorological Society*, **139**, pp 314-327. doi: 10.1002/qj.1944.

Stoffelen, A, 1998: Toward the true near-surface wind speed: error modelling and calibration using triple colocation. *Journal of Geophysical Research*, 7755-7766.

Torres, R., P. Snoiej, D. Geutner, D. Bibby, M. Davidson, E. Attema, P. Potin, B. Rommen, N. Floury, M. Brown et al., 2012: GMES Sentinel-1 mission. *Remote Sensing of Environment*, 120, 9-24.

TU Wien Remote Sensing Group, 2016: https://rs.geo.tuwien.ac.at/products/all/ascat/

Verhoest, N.E.C., P.A. Troch, C. Paniconi and P. De Troch, 1998: Mapping basin scale variable source areas from multitemporal remotely sensed observations of soil moisture behavior. *Water Resources Research,* **34**(12), 3235-3244.

Vinnikov, K.Y., A. Robock, N.A. Speranskaya and A. Schlosser, 1996: Scales of temporal and spatial variability of mid-latitude soil moisture. *Journal of Geophysical Research* **101**(D3): 7163-7174.

Wagner, W., G. Lemoine and H. Rott, 1999: A method for estimating soil moisture from ERS scatterometer and soil moisture data. *Remote Sensing of Environment*, **70**(2), 191-207.

Wagner, W., V. Naeimi, S. Cao, B. Bauer-Marchallinger, R. Kidd, S. Hasenauer, A. Dostalova and C. Paulik, 2016: The Use of Sentinel-1 for Monitoring of Soil Moisture within the Copernicus Global Land Service. *Proc. ESA Living Planet Symposium*, Prague, Czech Republic, 9-13 May 2016.

Yang, G.Y., Y.C. Shi and Q.Y. Xu, 2013: Estimation of Soil Moisture from Multi-Polarized Synthetic Aperture Radar Data-A Case Examination on RADARSAT-2 Product Over Wheat Growing Areas. *Sensor Letters*, **11** (6-7), 1081-1086.

Zribi, M., F. Kotti, R. Amri, W. Wagner, M. Shabou, Z. Lili-Chabaane and N. Baghdadi, 2014: Soil moisture mapping in a semiarid region, based on ASAR/Wide Swath satellite data. *Water Resources Research*, **50**(2), 823-835.

Zwieback, S., K. Scipal, W. Dorigo and W. Wagner, 2012: Structural and statistical properties of the collocation technique for error characterization. *Nonlinear Processes in Geophysics*, **19**, 69-80.